

Inverse Design of Discrete Interlocking Materials with Desired Mechanical Behavior

PENGBIN TANG, ETH Zürich, Switzerland

BERNHARD THOMASZEWSKI, ETH Zürich, Switzerland

STELIAN COROS, ETH Zürich, Switzerland

BERND BICKEL, ETH Zürich, Switzerland

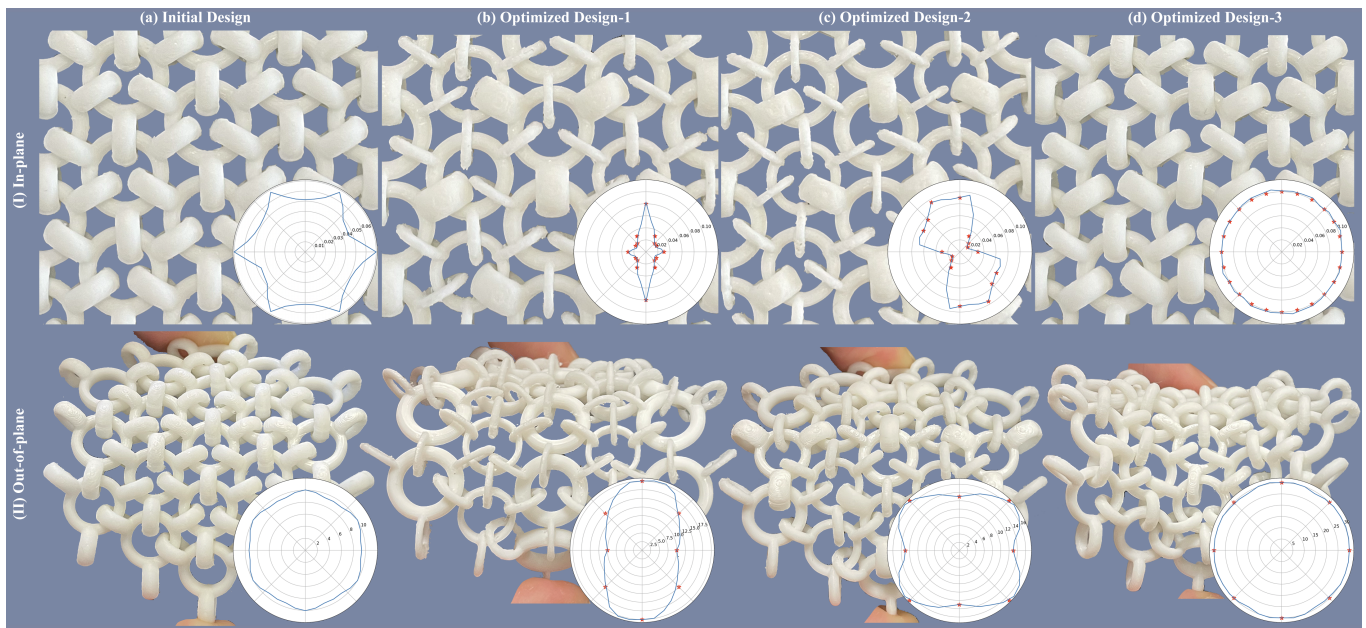


Fig. 1. Our method enables optimization-driven design of Discrete Interlocking Materials with desired mechanical behavior. For this threefold symmetric chainmail, both in- and out-of-plane mechanical properties of the initial homogeneous designs (I-a, II-a) exhibit threefold symmetric uniaxial deformation limit profiles. Our approach automatically finds shape parameters for each interlocking element that lead to diverse desired mechanical properties (red dots).

We present a computational approach for designing Discrete Interlocking Materials (DIMs) with desired mechanical properties. Unlike conventional elastic materials, DIMs are kinematic materials governed by internal contacts among elements. These contacts induce anisotropic deformation limits that depend on the shape and topology of the elements. To enable gradient-based design optimization of DIMs with desired deformation limits, we introduce an implicit representation of interlocking elements based on unions of tori. Using this low-dimensional representation, we simulate DIMs with smoothly evolving contacts, allowing us to predict changes in deformation limits as a function of shape parameters. With this toolset in hand, we optimize for element shape parameters to design heterogeneous DIMs that best approximate prescribed limits. We demonstrate the effectiveness of our method

by designing discrete interlocking materials with diverse limit profiles for in- and out-of-plane deformation and validate our method on fabricated physical prototypes.

CCS Concepts: • Computing methodologies → Modeling and simulation; Physical simulation; Collision detection; • Applied computing → Computer-aided design.

Additional Key Words and Phrases: Chainmail Fabric, Metamaterial, Incremental Potential Contact.

ACM Reference Format:

Pengbin Tang, Bernhard Thomaszewski, Stelian Coros, and Bernd Bickel. 2025. Inverse Design of Discrete Interlocking Materials with Desired Mechanical Behavior. In *Special Interest Group on Computer Graphics and Interactive Techniques Conference Conference Papers (SIGGRAPH Conference Papers '25)*, August 10–14, 2025, Vancouver, BC, Canada. ACM, New York, NY, USA, 11 pages. <https://doi.org/10.1145/3721238.3730675>

Please use nonacm option or ACM Engage class to enable CC licenses
This work is licensed under a Creative Commons Attribution 4.0 International License.
SIGGRAPH Conference Papers '25, August 10–14, 2025, Vancouver, BC, Canada
© 2025 Copyright held by the owner/author(s).
ACM ISBN 979-8-4007-1540-2/2025/08
<https://doi.org/10.1145/3721238.3730675>



1 INTRODUCTION

Designing materials that balance flexibility and strength is a central challenge for many engineering applications. Discrete interlocking materials (DIMs)—generalized chainmail fabrics made of quasi-rigid

interlocking elements—have shown promise in reconciling these traditionally opposing properties.

DIMs are highly flexible materials, allowing for deformations without restoring forces in their slack regime. The transition to the taut regime occurs upon full contact chain formation, activating the material’s inherent strength. This stark contrast in deformation response makes DIMs attractive for a diverse range of applications, ranging from robotics and biomedical devices to protective gear and aerospace engineering. Each of these applications will generally have specific requirements on material behavior, raising the question of how to design DIMs with desired mechanical properties. Unlike conventional elastic materials, DIMs are characterized by their kinematic deformation limits, which depend on the shape and topology of its constituent elements. The inverse design of DIMs with desired mechanical properties is challenging as element shapes with potentially large numbers of contacts have a complex, non-linear effect on material performance. Recently, Tang et al. [2023] introduced a homogenization algorithm to characterize in- and out-of-plane deformation limits of homogeneous DIMs by leveraging deformation tests via forward simulation.

In this work, we present a new computational approach for simulating and designing quasi-rigid discrete interlocking materials. Rather than using explicit triangle meshes, we propose an implicit representation based on unions of tori for simulating and designing discrete interlocking materials. Using this low-dimensional implicit representation, we simulate DIMs with smoothly evolving contacts, allowing us to predict changes in deformation limits as a function of shape parameters of interlocking elements. With this toolset in hand, we optimize for element shape parameters to design heterogeneous DIMs that best approximate prescribed macromechanical properties. We demonstrate the effectiveness of our method by designing DIMs with diverse limit profiles for in- and out-of-plane deformation. We further validate our method through real-world experiments on 3D-printed samples, showing good agreement between simulation and measurement.

2 RELATED WORK

Metamaterial Design. Through precisely architected microstructures, flexible metamaterials can achieve a broad range of macromechanical properties [Bertoldi et al. 2017]. Fueled by the increasing availability of 3D printing technology, the graphics community has started to embrace the problem of generating 3D-printable content such as models optimized for stability [Lu et al. 2014; Stava et al. 2012; Zhou et al. 2013], mechanical assemblies [Ceylan et al. 2013; Coros et al. 2013; Thomaszewski et al. 2014; Zhu et al. 2012], or characters that can be posed and deformed in desired ways [Bächer et al. 2012; Skouras et al. 2013]. One particular line of research in this context investigates the creation of 3D-printable metamaterials. The spectrum includes layered materials fabricated with multi-material printers [Bickel et al. 2010], materials with lattice-[Panetta et al. 2017, 2015], voxel- [Schumacher et al. 2015; Zhu et al. 2017], and foam-like [Martínez et al. 2016, 2017] structures, plate metamaterials [Ren et al. 2024; Rodriguez et al. 2022], as well as two-dimensional, sheet-like materials [Leimer and Musialski 2020; Li et al. 2023a; Martínez et al. 2019; Schumacher et al. 2018; Tozoni

et al. 2020]. While these previous works have explored many aspects of mechanical metamaterials, they all focus on elastic behavior. In this work, we introduce a computational method for designing a new class of metamaterials—discrete interlocking materials—whose behavior is regulated by internal contact, not elastic deformation. To our knowledge, no computational method has been introduced for designing DIMs.

Interlocking Materials & Structures. Using interlocking as a mechanism for creating stable assemblies is a concept that is used across architecture, robotics, and material sciences. This approach allows for the construction of functional furniture without nails or adhesives [Song et al. 2017; Sun et al. 2024; Yao et al. 2017], rigid assembly puzzles [Chen et al. 2022; Song et al. 2012; Sun and Zheng 2015; Wang et al. 2018; Xin et al. 2011], and stable surfaces made from flexible [Skouras et al. 2015] or rigid [Wang et al. 2019] components. Interestingly, imperfections during manufacturing can lead to loose joints such that assemblies, despite the rigidity of their components, can produce macroscopic deformations that can be harnessed, e.g., for robotics applications [Lensgraf et al. 2020]. Recently, Montes Maestre et al. [2024] considered flexible scaled sheets and introduced a computational approach for characterizing the complex coupling between quasi-rigid scales and the soft substrate in which they are embedded.

The concept of interlocking can also be used to create generalized chainmail materials with tunable mechanical behavior [Engel and Liu 2007; Ransley et al. 2017; Tang et al. 2023; Zhou et al. 2025]. For example, Wang et al. [2021] showed that vacuum-induced jamming is an effective way of controlling stiffness—a concept that has been further explored in multiple follow-up applications [Gao et al. 2023; Tian et al. 2023; Wang et al. 2023]. While these existing methods indicate a rich space of generalized chainmail materials, the question of how to determine parameters that lead to desired mechanical behavior remains largely open. In this work, we propose a new computational framework to simulate and design heterogeneous chainmail materials with desired macromechanical properties.

Simulating Contact. Contact modeling is crucial in science and engineering, particularly in applications such as robotics and computer animation. In the computer graphics community, robust contact simulation has been a focus for decades [Bertails-Descoubes et al. 2011; Erleben 2018; Geilinger et al. 2020; Kaufman et al. 2008; Li et al. 2022; Peiret et al. 2019]. In the context of simulating interlocking assemblies with tight contacts, Qu and James [2021] propose a method that computes certificates for topological validity between arrangements of closed curves found, e.g., when simulating knitwear [Cirio et al. 2014; Kaldor et al. 2008] or chainmail. For general contact simulation, the Incremental Potential Contact (IPC) method [Li et al. 2020] is a state-of-the-art contact model, utilizing clamped logarithmic barriers and continuous collision detection (CCD) to ensure intersection-free optimization. Subsequent work aimed at improving its robustness [Huang et al. 2024b; Li et al. 2023b] and performance [Huang et al. 2024a], and introduced extensions for implicit surfaces [Du et al. 2024] and rigid body motion [Ferguson et al. 2021]. Rigid-body IPC is a viable option for forward simulation of interlocking materials [Tang et al. 2023], although the computational costs can be substantial. For inverse design of generalized chainmail

materials, however, we observed that the combination of IPC and explicit triangle meshes becomes prohibitively expensive. To address this problem, we introduce an implicit representation of interlocking elements based on unions of tori. This implicit representation allows us to simulate discrete interlocking materials with smoothly evolving contacts, thus opening the door to efficient gradient-based design optimization of heterogeneous chainmail materials.

3 THEORY

Our goal is to design discrete interlocking materials (DIMs) with desired macromechanical properties. To this end, we must first be able to efficiently simulate DIMs and to compute the simulation derivatives required for inverse design. We focus on the design of kinematic deformation limits for DIMs made of quasi-rigid interlocking elements without considering friction or elasticity. To this end, we start by introducing an efficient implicit representation to model interlocking elements based on unions of tori. With this low-dimensional implicit representation, we simulate DIMs with smoothly evolving contacts, allowing us to predict changes in deformation limits as a function of shape parameters. Based on this efficient forward simulation, we formulate objective functions to optimize in- and out-of-plane deformation limits for heterogeneous DIMs with desired behavior.

3.1 Implicit Contact Model

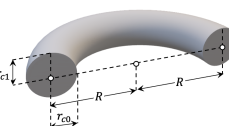
Torus-like rings are the typical building block for DIMs. They cover a large range of interlocking materials with diverse mechanical properties. We use an implicit representation to model each interlocking element based on unions of multiple tori with elliptical cross-sections. Any point on the surface of a given torus i can be parametrized as

$$\begin{aligned} V_x(\mathbf{c}_i) &= (R + r_{c0} \cos(v)) \cos(u), \\ V_y(\mathbf{c}_i) &= (R + r_{c0} \cos(v)) \sin(u), \\ V_z(\mathbf{c}_i) &= r_{c1} \sin(v), \end{aligned} \quad (1)$$

where $\mathbf{c}_i = (u, v)$ are 2D parametric coordinates, R is the ring radius of the torus, and r_{c0} and r_{c1} are the radii of the cross-section as shown in the inset figure. The squared distance between two surface points on the tori i and j can be defined as

$$d(\mathbf{c}_{ij}, \mathbf{q}_{ij}) = \|\mathbf{V}_i^t - \mathbf{V}_j^t\|^2, \quad (2)$$

where $\mathbf{c}_{ij} = (\mathbf{c}_i, \mathbf{c}_j)$ and $\mathbf{q}_{ij} = (\mathbf{q}_i, \mathbf{q}_j)$ are the parametric coordinates and rigid body configurations of torus i and j , respectively. Each rigid body configuration is given by $\mathbf{q}_i = (\mathbf{x}_i, \boldsymbol{\omega}_i) \in \mathbb{R}^6$, with translation \mathbf{x}_i and rotation $\boldsymbol{\omega}_i$. The transformed vertex position is $\mathbf{V}_i^t(\mathbf{c}_i, \mathbf{q}_i) = \mathbf{R}(\boldsymbol{\omega}_i)\mathbf{V}(\mathbf{c}_i) + \mathbf{x}_i$, where the position of vertex $\mathbf{V}(\mathbf{c}_i)$ is $\mathbf{V}(\mathbf{c}_i) = (V_x(\mathbf{c}_i), V_y(\mathbf{c}_i), V_z(\mathbf{c}_i))$, and the rotation matrix $\mathbf{R}(\boldsymbol{\omega}_i)$ is computed using Rodrigues' Rotation Formula, as described in [Ferguson et al. 2021]. To detect contact between two tori, we seek a pair of points, one on each torus, with minimum distance. Given the rigid transformations of the two tori, we obtain the minimum



squared distance by solving the minimization problem

$$\min_{\mathbf{c}_{ij}} d(\mathbf{c}_{ij}, \mathbf{q}_{ij}). \quad (3)$$

To this end, we use Newton's method with a convergence threshold of 10^{-12} on the distance gradient $\nabla_{\mathbf{c}_{ij}} d$. Furthermore, we reduce the gradient norm by taking full Newton steps until no further decrease is observed. Since the distance between two tori might have multiple local minima, we use multiple samples on both tori as initial guesses. If a local minimum squared distance satisfies $d < \hat{d}$, with $\hat{d} = 10^{-8}$, we add this contact pair into the contact set C and define a corresponding contact potential,

$$b(d, \hat{d}) = \begin{cases} -(d - \hat{d})^2 \ln(d/\hat{d}), & 0 < d < \hat{d}, \\ 0, & d \geq \hat{d}, \end{cases} \quad (4)$$

using the log barrier approach described in [Li et al. 2020]. With this implicit contact potential set up, we obtain static equilibrium states for all interlocking elements by solving the unconstrained minimization problem

$$\min_{\mathbf{q}} E = E_e + E_c, \quad (5)$$

where $\mathbf{q} = (\mathbf{q}_1, \dots, \mathbf{q}_n) \in \mathbb{R}^{6n}$ and $E_c = \mu \sum_{k \in C} b_k$ is the total contact potential summed over all contact pairs in the contact set C with an adaptive barrier stiffness μ as described in [Li et al. 2020]. Furthermore, E_e is the potential from external force defined in Equations (12) and (14) for in- and out-of-plane deformations, respectively. Section 1 of the supplementary document provides the analytical derivatives required for solving this minimization problem.

Continuous Collision Detection. Given a search direction from the linear solver, we must determine the step size α_t that reduces the objective function while avoiding intersections between interlocking elements. To this end, we develop a two-stage continuous collision detection (CCD) algorithm that takes advantage of broad and narrow phase detection schemes. In the broad phase, we approximate interlocking elements with bounding spheres and use a hash grid to efficiently detect overlaps. If two bounding spheres overlap, we add the corresponding interlocking elements to a candidate set for the narrow phase. In the narrow phase, we compute the largest step size α_t by finding the minimum squared distance between two tori, each belonging to different interlocking elements,

$$\min_{\alpha_t} d \quad (6a)$$

$$\text{s.t. } d(\alpha_t) = \min_{\mathbf{c}_{ij}} d(\mathbf{c}_{ij}, \mathbf{q}_{ij} + \alpha_t \Delta \mathbf{q}_{ij}) \quad (6b)$$

$$0 \leq \alpha_t \leq \alpha_{hi}. \quad (6c)$$

If $d < d_{th}$ with $d_{th} = 10^{-20}$, we flag the tori as intersecting and decrease α_{hi} by a factor of 0.9 until $d > d_{th}$. To solve the optimization problem (6), we apply sensitivity analysis to the optimality conditions $\nabla_{\mathbf{c}_{ij}} d = \mathbf{0}$ of (6b),

$$\nabla_{\mathbf{c}_{ij}}^2 d \cdot \frac{d\mathbf{c}_{ij}}{d\mathbf{q}_{ij}} + \frac{\partial^2 d}{\partial \mathbf{c}_{ij} \partial \mathbf{q}_{ij}} = \mathbf{0}, \quad (7)$$

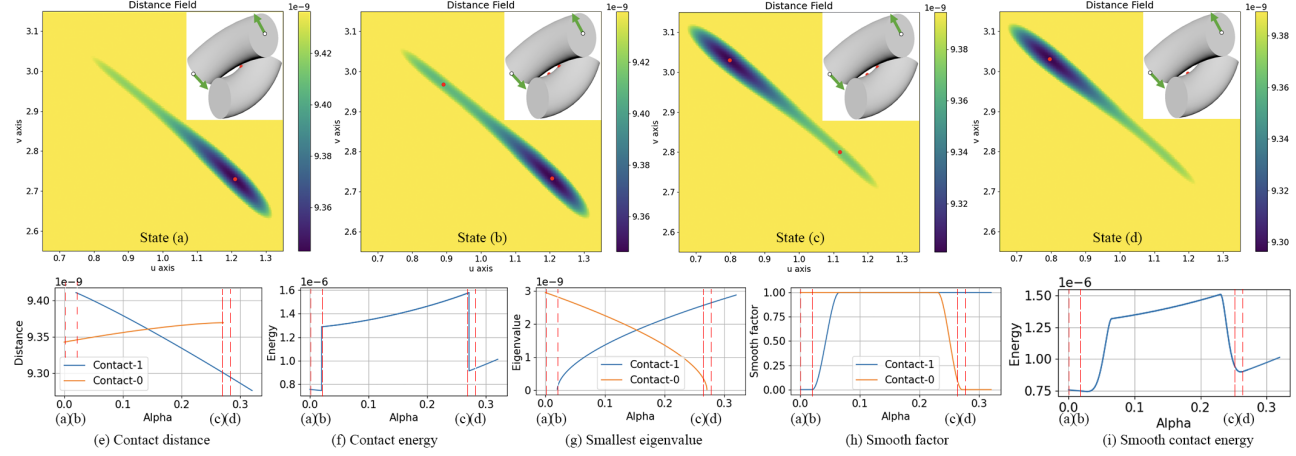


Fig. 2. Singularity of contact between two tori. States (a-d) are four different contact states with increasing line search step size, each of which presents the minimum squared distance field of a torus to the other torus in $u - v$ coordinate. For the sake of clarity, we show the color of the distance field between minimum distance d_m and $101\% d_m$. (a) Given $\hat{d} = 10^{-8}$, there is only one pair of contact points between two tori at the beginning. (b) Increasing a tiny step size, the torus rotates and the second pair of contact points suddenly emerges, leading to an energy wall; see the left side of (f). (c) The ‘contact zone’ gradually transitions from contact-0 to contact-1. (d) Further increasing the step size to around 0.27, the contact-0 disappears, resulting in a discontinuous energy drop; see the right side of (f). (e) The evolving distance of the two contact pairs, where contact-0 and -1 disappear and emerge with a squared distance smaller than \hat{d} , respectively, resulting in a discontinuous contact energy contribution. (g) Our key observation is that the smallest eigenvalue of contact-0 smoothly decreases from 2.95×10^{-9} to 0 and the smallest eigenvalue of contact-1 increases from 0 to 2.87×10^{-9} . (h) By leveraging the smallest eigenvalue, we can compute a smooth factor leading to a smooth change in contact energy (i).

from which we compute the sensitivity matrix $\frac{dc_{ij}}{dq_{ij}}$. The gradient of the objective function then follows as

$$\nabla_{\alpha_t} d = \left(\frac{\partial d}{\partial c_{ij}} \frac{dc_{ij}}{dq_{ij}} + \frac{\partial d}{\partial q_{ij}} \right) \frac{dq_{ij}}{d\alpha_t}. \quad (8)$$

There can exist multiple local minima when solving Equation (6b) for a given step size α_t . Similar to the approach used for solving Equation (3), we therefore use multiple sampling points to identify these minima and select the one with the smallest function value to compute the sensitivity matrix $\frac{dc_{ij}}{dq_{ij}}$. As we discuss below, there can be situations in which the contact coordinates of the smallest minimum distance change discontinuously as a function of the tori’s configurations; see Figure 2(e). In such cases, the global minimum distance is only C^0 -continuous. However, since we can always track the closest distance between two tori in contact, we can simply use step size reduction during line search to prevent intersections. Ultimately, we can efficiently solve Equation (6) as a 1-dimensional bound-constrained minimization problem for all tori in the candidate set in parallel using L-BFGS-B.

3.2 Singularity

The minimum distances computed from the implicit representation of tori can yield multiple contact points. In instances where two tori are stacked parallel, their contact manifests as a circumferential ridge, leading to a null space in the distance minimization problem. However, when modeling DIMs where each torus interlocks with others, this type of singularity does not arise. Another potential singularity arises when one torus passes through the center of another torus, resulting in a circular region of equal distance. In

practice, however, interlocking tori must have clearance values larger than \hat{d} to allow for sufficient kinematic mobility. We therefore constrain the thickness of tori accordingly by imposing bounds on cross-section variables. Consequently, this second type of singularity can only arise at distances larger than \hat{d} , but such contact pairs are filtered out anyway.

While these two types of singularities present no problem in practice, the third type is more challenging to deal with. Specifically, when two interlocking tori rotate relative to one another, we observe a shift in the number of contact pairs—from one to two or from two to one—with each of them starting or ending with a squared distance smaller than \hat{d} . As shown in Figure 2, a second contact pair suddenly appears or disappears during relative rotations between the tori. If a candidate step leads to such a change in contact pairs, the energy changes abruptly (Figure 2(f)) and the step will likely be rejected.

To address this problem, we must be able to detect this singularity problem and introduce a smoothly evolving variable for contact so that we can leverage it to build a smoothly changing contact energy. Our key observation is that the smallest eigenvalue λ_k of the Hessian matrix in the distance minimization problem (3) increases smoothly from 0 with the appearance of k -th contact pair in the contact set C as shown in Figure 2(g). This allows us to introduce a smooth factor to compute a continuous and differentiable energy by a polynomial function,

$$h_k = \begin{cases} -(n-1) \frac{\lambda_k}{\bar{\lambda}}^n + n \frac{\lambda_k}{\bar{\lambda}}^{n-1}, & 0 \leq \lambda_k \leq \bar{\lambda}, \\ 1, & \lambda_k > \bar{\lambda}, \\ 0, & \lambda_k < 0. \end{cases} \quad (9)$$

We use $n = 5$ and $\bar{\lambda} = 10^{-9}$, resulting in the plot shown in the inset. It is worth noting that since contact points exist at locations with local minimum distances, the smallest eigenvalue is always $\lambda \geq 0$. Furthermore, from our observation, the smallest eigenvalue is unique within the given range. This smooth factor h_k can lead to a smooth energy transition from one to two contact points, as shown in Figure 2(i). However, a contact point with a small eigenvalue will lead to a small factor, resulting in a small contact energy contribution even if the contact distance is small. This can lead to an ill-conditioned optimization problem and potential intersections. To this end, we further introduce a polynomial smooth factor depending on both the contact squared distance d and the factor h_k as

$$s_k(d, h_k) = \begin{cases} h_k \cdot d'^2(3 - 2d') + (1 - d')^2(1 + 2d') , & d_1 \leq d \leq d_2 , \\ 1 , & d < d_1 , \\ h_k , & d > d_2 , \end{cases} \quad (10)$$

where $d' = \frac{d - d_1}{d_2 - d_1}$ with $d_1 = 10^{-12}$ and $d_2 = 4 \times 10^{-12}$; see the function plot on the right inset figure. This function smoothly transitions from h_k to 1 if the distance of a contact pair gets smaller than the threshold d_2 , thus, avoiding a tiny distance and intersections. With this modification, we rewrite the contact potential in Equation (5) as

$$E_c = \mu \sum_{k \in C} s_k b_k . \quad (11)$$

Leveraging the smooth evolving contact potential, our method can robustly predict the deformation behaviors of DIMs. This implicit simulation model is then utilized for the design of heterogeneous DIMs in the following section.

3.3 Inverse Design of Mechanical Properties

The implicit contact model offers an efficient forward simulation of DIMs. Furthermore, it provides smooth gradient information to the optimization-driven method for the inverse design of DIMs with various in- and out-of-plane deformation limits.

In-plane deformation limits. We design the in-plane behavior of DIMs on a tileable unit cell with in-plane periodic boundary conditions, as shown in Figure 3(a). These require $x_j = x_i + t_{ij}(\epsilon)$ for translation and $\omega_i = \omega_j$ for rotation. Analogous conditions are applied to the second boundary pair, i.e., $x_k = x_i + t_{ik}(\epsilon)$ and $\omega_k = \omega_i$, where t_{ij} and t_{ik} are both a function of the in-plane strain $\epsilon = (\epsilon_x, \epsilon_y, \epsilon_{xy})^T$. Specifically, for example, t_{ij} is defined as $t_{ij} = \overline{Ft_{ij}}$, where $F = U(\epsilon) + I$ is the 2×2 symmetric deformation gradient, with U being the pure stretch strain tensor—excluding any rotational component—constructed from ϵ , and $\overline{t_{ij}}$ is the translation in the rest state. Therefore, the material configuration under a given macroscopic target strain $\hat{\epsilon}$ can be determined by solving the

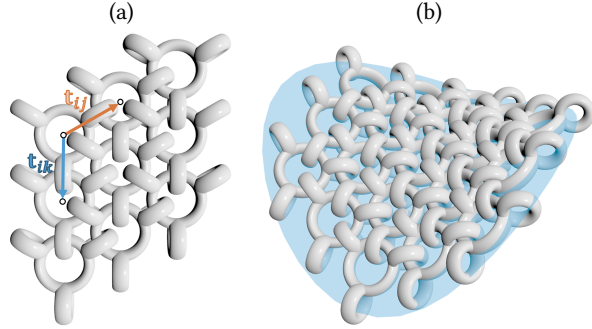
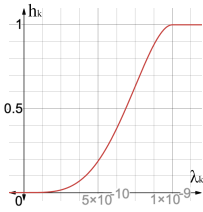


Fig. 3. We follow [Tang et al. 2023] and use (a) in-plane periodic boundary conditions and (b) a paraboloid surface to capture the in- and out-of-plane deformation limits, respectively.

following unconstrained optimization problem,

$$\min_y E_{\text{planar}} = \frac{1}{2}(\epsilon - \hat{\epsilon})^2 + E_c(y) , \quad (12)$$

where $y = (q, \epsilon)^T$. In order to capture the in-plane deformation limits, we set a large unreachable value as the macroscopic target strain $\hat{\epsilon}$, from which we can obtain the boundary strain ϵ in a specified direction θ_i .

For the specified target in-plane deformation limit $\epsilon_t(\theta_i)$ in direction θ_i , therefore, we define the design objective function for in-plane deformation limits as

$$\begin{aligned} \min_p T &= \sum_i \frac{1}{2}(\epsilon(p, \theta_i) - \epsilon_t(\theta_i))^2 \\ \text{s.t. } f_{\text{planar}}(y(p), p, \theta_i) &= 0 , \forall i \\ C_{ij}(p) &> \epsilon_c , \forall (i, j) \in N \\ \epsilon_l < p < \epsilon_h , \end{aligned} \quad (13)$$

where $p = (p_1, \dots, p_n)$ is the design parameters of all interlocking elements with each of them as $p_i = (t_0, \dots, t_k)$ and each torus as $t_k = (r_{c0}, r_{c1}, R)$, $y = (q, \epsilon)^T$ is a function of design parameters p , $f_{\text{planar}}(y(p), p, \theta_i) = 0$ is the static equilibrium constraints by solving Equation (12) in direction θ_i , the constraints $C_{ij}(p)$ are used to guarantee the cross-section of torus j is smaller than the hole of its neighbor interlocking element i with a threshold ϵ_c for all tori in the neighbor information set N . For example, to guarantee the cross-section of a torus is smaller than its interlocking torus belonging to another interlocking element, we write $C_{ij}(p) = R_i - r_{c0i} - \max(r_{c0j}, r_{c1j})$. In order to get a continuous constraint Jacobian, here, we split it into two constraints, i.e., $R_i - r_{c0i} - r_{c0j} > \epsilon_c$ and $R_i - r_{c0i} - r_{c1j} > \epsilon_c$. Furthermore, all design parameters are constrained within a printable range (ϵ_l, ϵ_h) .

Out-of-plane deformation limits. We characterize the out-of-plane behavior of DIMs by asking a given circular patch of interlocking elements to fit the target paraboloid surface $z = Ax^2 + By^2 + Cxy$ with prescribed curvatures $\kappa = (A, B, C)^T$, as shown in Figure 3(b). This requires all the positions of elements to satisfy $x_i(\kappa) = (x_i, y_i, Ax_i^2 + By_i^2 + Cxy_i)$. Similar to the in-plane case, we set a large unreachable target bending curvature $\hat{\kappa}$ to find the out-of-plane deformation

limits κ by solving the minimization problem

$$\min_{\mathbf{y}} E_{\text{bending}} = \frac{1}{2}(\boldsymbol{\kappa} - \hat{\boldsymbol{\kappa}})^2 + E_c(\mathbf{y}), \quad (14)$$

where $\mathbf{y} = (\mathbf{q}, \boldsymbol{\kappa})^T$. Once the out-of-plane deformation limits are determined across multiple prescribed directions, we define the out-of-plane design objective function as

$$\begin{aligned} \min_{\mathbf{p}} T &= \sum_i \frac{1}{2}(\boldsymbol{\kappa}(\mathbf{p}, \theta_i) - \boldsymbol{\kappa}_t(\theta_i))^2 \\ \text{s.t. } &\mathbf{f}_{\text{bending}}(\mathbf{y}(\mathbf{p}), \mathbf{p}, \theta_i) = \mathbf{0}, \forall i \\ &C_{ij}(\mathbf{p}) > \epsilon_c, \forall (i, j) \in \mathcal{N} \\ &\epsilon_l < \mathbf{p} < \epsilon_h, \end{aligned} \quad (15)$$

where $\boldsymbol{\kappa}_t(\theta_i)$ is the prescribed target out-of-plane deformation limit in direction θ_i , $\mathbf{f}_{\text{bending}}(\mathbf{y}(\mathbf{p}), \mathbf{p}, \theta_i) = \mathbf{0}$ is the static equilibrium constraints by solving Equation (14) in direction θ_i with $\mathbf{y} = (\mathbf{q}, \boldsymbol{\kappa})^T$ for the out-of-plane case.

Optimization. The above inverse design problems can be expressed with the following general form,

$$\begin{aligned} \min_{\mathbf{p}} &T(\mathbf{y}(\mathbf{p}), \mathbf{p}) \\ \text{s.t. } &\mathbf{f}(\mathbf{y}(\mathbf{p}), \mathbf{p}, \theta_i) = \mathbf{0}, \forall i, \\ &C_{ij}(\mathbf{p}) > \epsilon_c, \forall (i, j) \in \mathcal{N}, \\ &\epsilon_l < \mathbf{p} < \epsilon_h, \end{aligned} \quad (16)$$

where the variables \mathbf{y} are the state of the DIM, which is a function of design parameters \mathbf{p} , $\mathbf{f}(\mathbf{y}(\mathbf{p}), \mathbf{p}, \theta_i) = \mathbf{0}$ is the static equilibrium constraints. We solve this constrained optimization problem using a Sequential Quadratic Programming (SQP) algorithm with a backtracking line search and set a threshold of 10^{-2} as the condition for convergence. We compute the gradient of the design objective as

$$\frac{dT}{d\mathbf{p}} = \frac{\partial T}{\partial \mathbf{y}} \frac{d\mathbf{y}}{d\mathbf{p}} + \frac{\partial T}{\partial \mathbf{p}}, \quad (17)$$

where $\frac{d\mathbf{y}}{d\mathbf{p}}$ can be computed from the sensitivity analysis as described in Section 2 of the supplementary document. For the Hessian of the inverse design problems, it is hard to compute and will be very indefinite, we use the BFGS algorithm to approximate a positive definite Hessian. To increase the robustness of the QP solver, we further enforce the Hessian to be positive definite by shifting all negative eigenvalues to 10^{-6} .

Parameter-CCD. After obtaining the search direction from the QP solver, we must ensure that there are no intersections when changing design parameters during line search. Similar to the CCD approach described above, we also develop a parameters-CCD to prevent intersections while optimizing design parameters \mathbf{p} , using similar broad- and narrow-phase procedures.

4 RESULTS

We evaluate our method on a set of discrete interlocking materials. We start by describing our experimental setup, after which we compare the performance of forward simulation between our method and IPC with explicit meshes. Finally, we present multiple

Table 1. Performance comparison between our implicit method and IPC with explicit triangle meshes for forward simulation. The threefold, fourfold, and chainmail examples correspond to the material shown in Figure 5(l-a), 7(a), and 8(a), respectively. #Tori indicates the number of tori in the unit cell.

Example	#Tori	Ours [s]	IPC [s]	Speedup
Threefold	16	2.134	29.287	13.7x
Fourfold	18	12.375	56.325	4.6x
Chainmail	8	5.444	41.745	7.7x

designs optimized by our approach and validate our method with corresponding physical prototypes.

Experimental Setup. We fabricate all samples using an FDM printer with water-dissolvable support. To validate the in-plane deformation limits, we stretch and compress samples along a given direction 3 times. Similar to Tang et al. [2023], we report a Cauchy strain-like relative measure $\eta = \frac{\epsilon_s - \epsilon_c}{1 + \epsilon_c}$ in our plots, where ϵ_s and ϵ_c are stretching and compression deformation limits. For the out-of-plane deformation limits, we qualitatively compare our simulation results to the corresponding physical prototypes under external uniaxial bending.

Comparing to IPC with Explicit Meshes. We compare the performance of our implicit method to IPC with explicit meshes as shown in Table 1. We start from the same initial configuration and compute the state of the in-plane deformation limit of periodic materials under stretching in 0 degrees. Note that the boundary interlocking elements will collide with elements on the other side of the boundary due to periodicity, so we duplicate the unit cell elements for contact purposes in both our method and IPC with explicit meshes. We solve the static equilibrium state with a convergence threshold 10^{-8} for Newton’s method. We use $\hat{d} = 10^{-8}$ and set the adaptive barrier stiffness μ as the same fixed value. For IPC with explicit meshes, we use a regular mesh with a resolution of 20×20 for each torus. As can be seen from the performance comparison, our method provides a significant speedup. In addition to the performance comparison, we further validate our method by computing the error of the explicit mesh with IPC relative to our method at the state of the in-plane deformation limit, as shown in Figure 4. The results demonstrate that the rigid body configuration converges to the solution computed from our method as the mesh resolution increases. These examples were tested on a machine with an Apple M3 Pro processor and 36 GB of RAM.

Threefold Symmetric Chainmail. Our first example is the threefold symmetric chainmail as shown in Figure 1 and 5. Each element of this material connects to its six immediate neighbors, leading to an overall threefold symmetric structure for the initial homogeneous design; see Figure 5(l-a). This initial design exhibits the same threefold symmetric limit profile for in-plane deformations. For the inverse design, we use 2 by 2 elements as the unit cell, and each element is represented by 6 parameters, i.e., 3 parameters for the center torus and three-side tori sharing the remaining 3 parameters.

Using the initial homogeneous design as the starting point, we first fit its uniaxial profile to seemingly challenging orthotropic

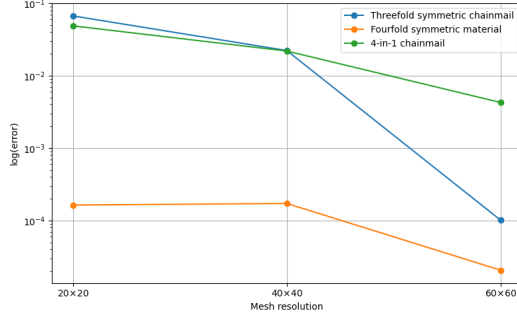


Fig. 4. Rigid body configuration error of the explicit mesh with IPC compared to our method at the in-plane deformation limit.

and anisotropic profiles for this threefold symmetric material. Our method can effectively find the prescribed targets as shown in Figure 1(I-b) and (I-c). We then optimize it to an isotropic uniaxial deformation limit with higher bounds as shown in Figure 1 (I-d) and 5(I-d). Interestingly, the material profile with larger in-plane isotropic deformation limits presents a subtle visual difference to the initial design. To validate the effectiveness of our inverse design algorithm, we measure the physical prototypes in multiple directions. As can be seen from the strain plots in Figure 5(I), the simulation results (blue) show a good agreement with the experimental data (orange).

For out-of-plane cases, we employ the same initial homogeneous pattern and optimize uniaxial bending curvatures on a disk patch as shown in the inset. This initial design presents an almost isotropic uniaxial bending profile. Utilizing the same design parameters as the in-plane case, our method can effectively find the desired orthotropic and isotropic uniaxial bending deformation limits with much higher curvatures as shown in Figure 5 (II). We validate the out-of-plane behavior qualitatively by comparing the simulation results with the fabricated physical prototypes. As can be seen from Figure 6, the simulation results closely track the bending behavior of physical prototypes for all the designs.

Fourfold symmetric Material. Our second example is a fourfold symmetric material made from elements with three orthogonal tori, as shown in Figure 7 (a). As can be seen from the uniaxial strain plot, this initial homogeneous design exhibits a fourfold symmetric profile. Using 6 elements as the unit cell, with each element sharing the same 3 parameters of a torus, we first try to optimize its uniaxial deformation limits to isotropic as shown in Figure 7 (b). The optimized uniaxial deformation limits for design-1 closely match the prescribed targets only with a small difference. We then try to optimize an orthotropic profile that has lower deformation limits in the diagonal directions and similar deformation limits at 0 and 90 degrees. Our inverse design algorithm successfully finds the specified properties. We further optimize this material to an anisotropic uniaxial profile, and our method finds the corresponding design that closely matches the targets as shown in Figure 7(d). We measure the

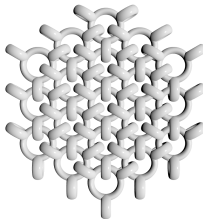


Table 2. Statistics for inverse design examples in Figure 5, 7, and 8. The columns list the number of tori in the simulation (#Tori), the number of parameters used in optimization (#Parameters), the number of fitting directions (#Direction), the number of iterations for the inverse design (#Iter), and the average time per iteration for the inverse design.

Example	#Tori	#Parameters	#Directions	#Iter	Avg. time[s]
Threefold (I-b)	16	24	16	243	62.8
Threefold(I-c)	16	24	16	112	99.5
Threefold(I-d)	16	24	24	66	104.7
Threefold(II-b)	76	24	4	129	28.4
Threefold(II-c)	76	24	4	115	36.2
Threefold(II-d)	76	24	4	107	16.8
Fourfold(b)	18	18	16	82	226.9
Fourfold(c)	18	18	16	110	137.6
Fourfold(d)	18	18	16	112	216.7
Chainmail(b)	8	24	16	37	411.1
Chainmail(c)	8	24	12	53	282.9
Chainmail(d)	8	24	12	40	342.7

deformation limits of this material at 0 and 90 degrees, all of these simulation results show a good agreement with the experimental measurements.

4-in-1 Chainmail. As the third example, we design the in-plane behavior of classic chainmail as shown in Figure 8. In the inverse design, using 8 tori as the unit cell, with each having 3 parameters, we first optimize to an orthotropic deformation limit, which has similar tight bounds in 0 degrees but admits much larger deformation from 45 to 135 degrees. As can be seen from Figure 8(b), our inverse design algorithm can successfully optimize the uniaxial deformation limits to the specified orthotropic profile only with small deviations to the targets. We then extend the orthotropic profile to an anisotropic version with different limits in two diagonal directions. Our inverse design algorithm can effectively find the specified targets in Figure 8(c). Our final design is to fit an isotropic behavior for the chainmail, our method optimizes to a locally optimal solution with a larger deviation at 30 degrees. However, as can be seen from Figure 8(d), the deformation limit in 0 degrees increases about 4 times larger than the initial design as prescribed in the target.

Performance & Statistics. All the inverse design examples run on a cloud computing service equipped with an AMD EPYC 7742 with 2.25 GHz. Statistics are given in Table 2.

5 CONCLUSIONS

We presented a method for the inverse design of discrete interlocking materials with desired mechanical properties. Rather than simulating using explicit meshes, we proposed an efficient low-dimensional implicit contact model based on unions of tori to predict the macromechanical properties of DIMs. Using this computational model, we developed optimization-driven methods to inverse design DIMs with desired in- and out-of-plane mechanical properties. We applied our method to a set of DIMs and validated our results

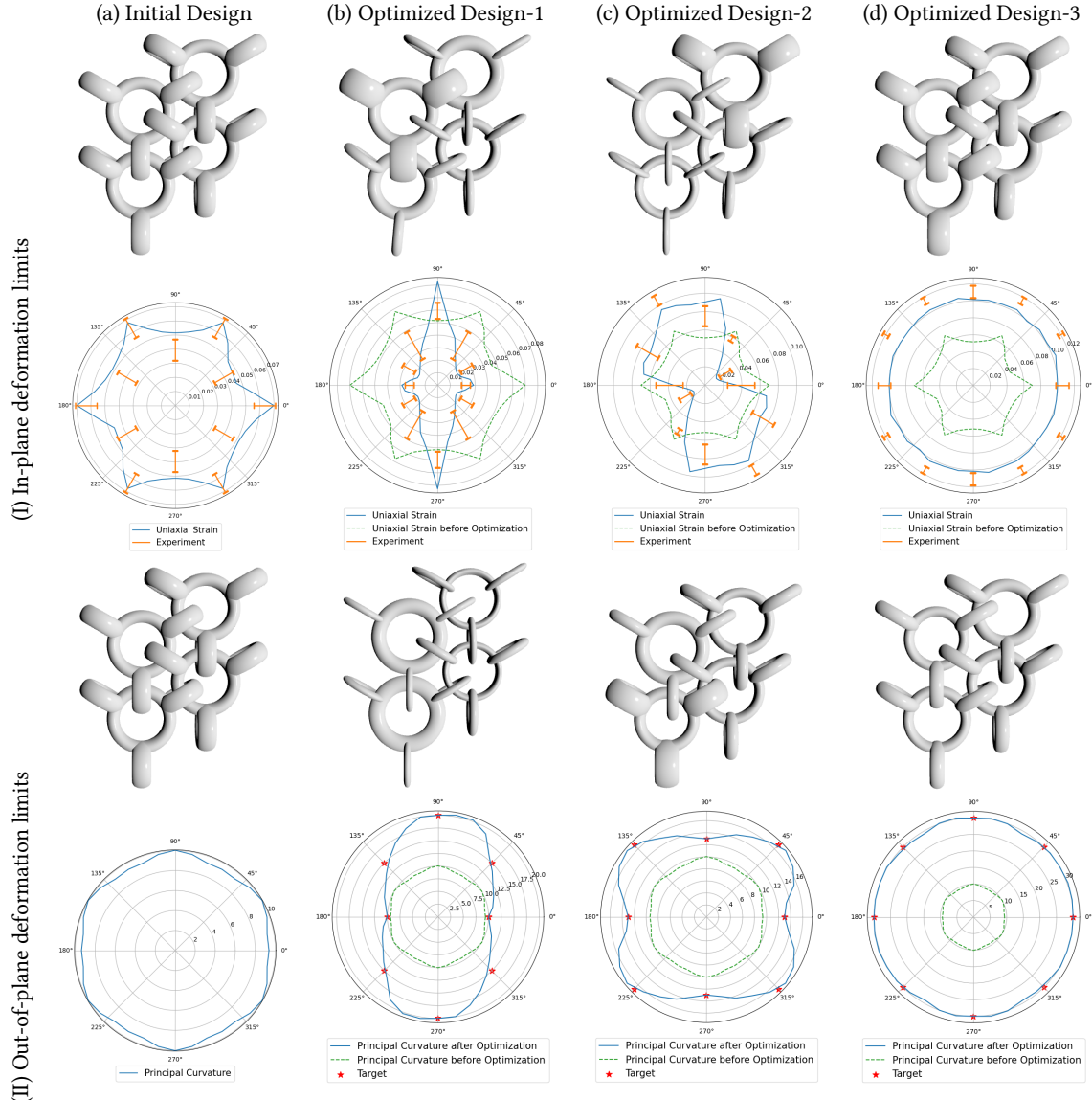


Fig. 5. Threefold symmetric chainmail.

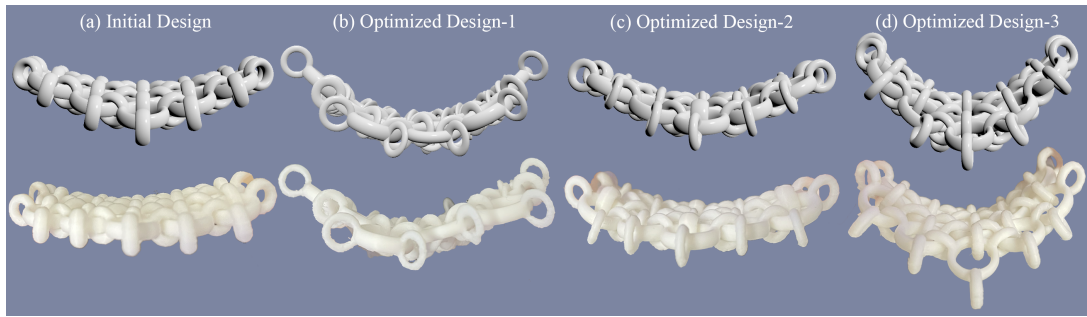


Fig. 6. Comparison of bending behaviors between simulation and physical prototypes.

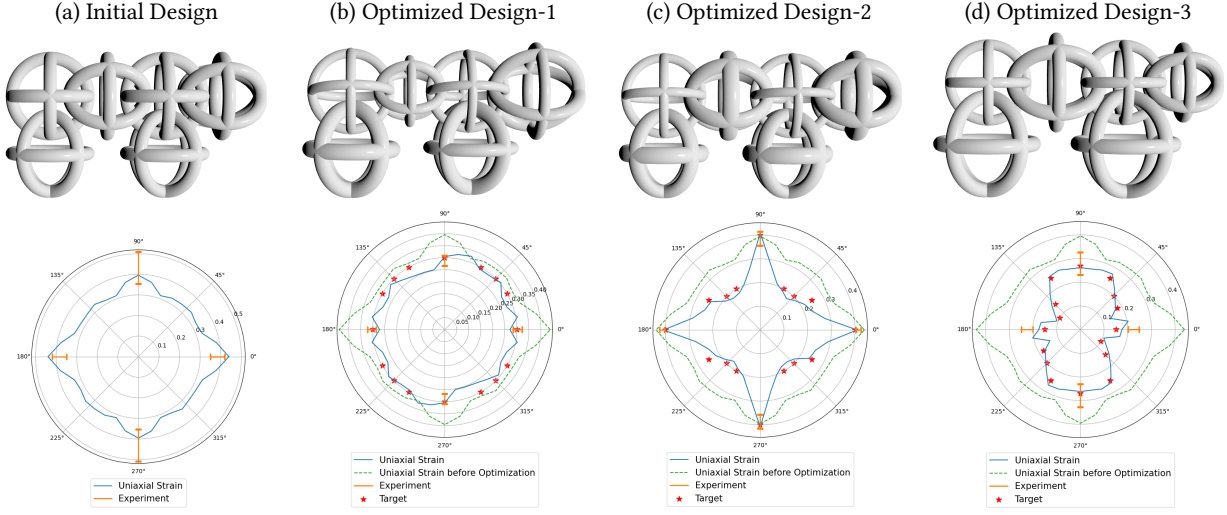


Fig. 7. Fourfold symmetric material.

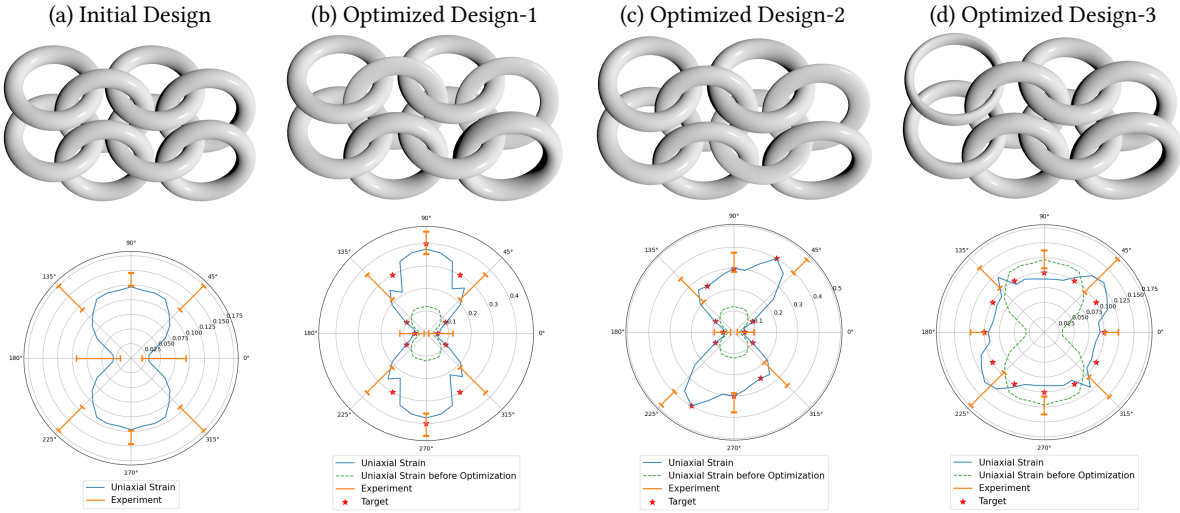


Fig. 8. 4-in-1 chainmail.

against measurements on physical prototypes. The various designed DIMs in the results show a good agreement with the experimental measurement.

5.1 Limitations & Future Work

Our method has several limitations that indicate avenues for future work. We focus on the torus as the basic building block for DIMs. However, many other types of DIMs are not made of unions of tori. Our implicit contact model is general and can be easily extended for simulating and designing DIMs with other types of parametric models.

Our formulation for singularity does not guarantee smooth contact energy when the second contact point emerges with a contact distance $d < d_2$ and the corresponding smallest eigenvalue $\lambda = 0$.

However, in our experiments, the smooth formulations perform well in both forward simulation and inverse design problems. Notably, without the introduced smooth formulation, Newton's method fails to compute a static equilibrium state, as no feasible step size can be found that ensures decreasing energy. In the future, developing new smooth contact formulations for implicit surfaces will be an interesting direction.

Our CCD does not have formal robustness guarantees that our method will always find the first close contact in the time interval. However, we never encountered a case where we missed an earlier contact in our experiments. Since tori are relatively well-behaved geometric shapes without sharp or non-smooth features, constraining the step size to be within the radii of the two tori can reliably allow us to find the earliest contact.

Our method focuses on the design of DIMs with desired kinematic deformation limits and models elements as rigid bodies without considering elasticity and friction. This is an idealized assumption. Developing new efficient methods capable of capturing elastic deformation for designing DIMs is an interesting direction for future research. Furthermore, for DIMs with tight contact, friction force can become dominant and lead to different macromechanical properties. As shown by Wang et al. [2021], resistance to deformation can be controlled through normal pressure—a mechanism which crucially relies on friction. In the future, adding friction into the contact model for designing these contact-dominated materials will be an interesting direction.

Our method can be applied to design two-dimensional DIMs. As indicated by Zhou et al. [2025], DIMs can be structured as three-dimensional architected materials for various applications. Our method can be easily extended for simulating these 3D architected materials. Exploring new methods for designing them will be a worthwhile direction for future work.

Finally, we have developed a new method for designing the mechanical properties of heterogeneous DIMs. In the future, we would like to design and simulate heterogeneous materials with curved shapes and spatially varying connectivities.

ACKNOWLEDGMENTS

The authors thank anonymous reviewers for their valuable feedback. We are also grateful to Rafael Bischof for proofreading the paper. This work was supported by the European Research Council (ERC) under the European Union’s Horizon 2020 research and innovation program (grant agreement No. 866480), and the Swiss National Science Foundation through SNF project grant 200021_200644.

REFERENCES

- Moritz Bächer, Bernd Bickel, Doug L. James, and Hanspeter Pfister. 2012. Fabricating Articulated Characters from Skinned Meshes. *ACM Trans. Graph.* 31, 4, Article 47 (jul 2012), 9 pages. <https://doi.org/10.1145/2185520.2185543>
- Florence Bertails-Descoubes, Florent Cadoux, Gilles Daviet, and Vincent Acary. 2011. A Nonsmooth Newton Solver for Capturing Exact Coulomb Friction in Fiber Assemblies. *ACM Trans. Graph.* 30, 1, Article 6 (feb 2011), 14 pages. <https://doi.org/10.1145/1899404.1899410>
- Katia Bertoldi, Vincenzo Vitelli, Johan Christensen, and Martin Van Hecke. 2017. Flexible mechanical metamaterials. *Nature Reviews Materials* 2, 11 (2017).
- Bernd Bickel, Moritz Bächer, Miguel A. Otaduy, Hyunho Richard Lee, Hanspeter Pfister, Markus Gross, and Wojciech Matusik. 2010. Design and fabrication of materials with desired deformation behavior. *ACM Trans. Graph.* 29, 4, Article 63 (July 2010), 10 pages. <https://doi.org/10.1145/1778765.1778800>
- Duygu Ceylan, Wilmot Li, Niloy J. Mitra, Maneesh Agrawala, and Mark Pauly. 2013. Designing and fabricating mechanical automata from mocap sequences. *ACM Trans. Graph.* 32, 6, Article 186 (Nov. 2013), 11 pages. <https://doi.org/10.1145/2508363.2508400>
- Rulin Chen, Ziqi Wang, Peng Song, and Bernd Bickel. 2022. Computational design of high-level interlocking puzzles. *ACM Trans. Graph.* 41, 4, Article 150 (July 2022), 15 pages. <https://doi.org/10.1145/3528223.3530071>
- Gabriel Cirio, Jorge Lopez-Moreno, David Miraut, and Miguel A. Otaduy. 2014. Yarn-Level Simulation of Woven Cloth. *ACM Trans. Graph.* 33, 6, Article 207 (nov 2014), 11 pages. <https://doi.org/10.1145/2661229.2661279>
- Stelian Coros, Bernhard Thomaszewski, Gioacchino Noris, Shinjiro Sueda, Moira Forberg, Robert W. Sumner, Wojciech Matusik, and Bernd Bickel. 2013. Computational Design of Mechanical Characters. *ACM Trans. Graph.* 32, 4, Article 83 (jul 2013), 12 pages. <https://doi.org/10.1145/2461912.2461953>
- Y. Du, Y. Li, S. Coros, and B. Thomaszewski. 2024. Robust and Artefact-Free Deformable Contact with Smooth Surface Representations. *Computer Graphics Forum* 43, 8 (2024), e15187. <https://doi.org/10.1111/cgf.15187> arXiv:<https://onlinelibrary.wiley.com/doi/10.1111/cgf.15187>
- Jonathan Engel and Chang Liu. 2007. Creation of a metallic micromachined chain mail fabric. *Journal of Micromechanics and Microengineering* 17, 3 (feb 2007), 551. <https://doi.org/10.1088/0960-1317/17/3/018>
- Kenny Erleben. 2018. Methodology for Assessing Mesh-Based Contact Point Methods. *ACM Trans. Graph.* 37, 3, Article 39 (jul 2018), 30 pages. <https://doi.org/10.1145/3096239>
- Zachary Ferguson, Minchen Li, Teseo Schneider, Francisca Gil-Ureta, Timothy Langlois, Chenfanfu Jiang, Denis Zorin, Danny M. Kaufman, and Daniele Panozzo. 2021. Intersection-free rigid body dynamics. *ACM Trans. Graph.* 40, 4, Article 183 (July 2021), 16 pages. <https://doi.org/10.1145/3450626.3459802>
- Weinan Gao, Jingtian Kang, Guohui Wang, Haoxiang Ma, Xueyan Chen, Muamer Kadic, Vincent Laude, Huirong Tan, and Yifan Wang. 2023. Programmable and Variable-Stiffness Robotic Skins for Pneumatic Actuation. *Advanced Intelligent Systems* 5, 12 (2023), 2300285. <https://doi.org/10.1002/aisy.202300285> arXiv:<https://advanced.onlinelibrary.wiley.com/doi/pdf/10.1002/aisy.202300285>
- Moritz Geilinger, David Hahn, Jonas Zehnder, Moritz Bächer, Bernhard Thomaszewski, and Stelian Coros. 2020. ADD: Analytically Differentiable Dynamics for Multi-Body Systems with Frictional Contact. *ACM Trans. Graph.* 39, 6, Article 190 (nov 2020), 15 pages. <https://doi.org/10.1145/3414685.3417766>
- Kemeng Huang, Floyd M. Chitalu, Huancheng Lin, and Taku Komura. 2024a. GIPC: Fast and Stable Gauss-Newton Optimization of IPC Barrier Energy. *ACM Trans. Graph.* 43, 2, Article 23 (March 2024), 18 pages. <https://doi.org/10.1145/3643028>
- Zizhou Huang, Max Paik, Zachary Ferguson, Daniele Panozzo, and Denis Zorin. 2024b. Orientation-aware Incremental Potential Contact. *arXiv preprint arXiv:2402.00719* (2024).
- Jonathan M. Kaldor, Doug L. James, and Steve Marschner. 2008. Simulating Knitted Cloth at the Yarn Level. In *ACM SIGGRAPH 2008 Papers* (Los Angeles, California) (*SIGGRAPH ’08*). Association for Computing Machinery, New York, NY, USA, Article 65, 9 pages. <https://doi.org/10.1145/1399504.1360664>
- Danny M. Kaufman, Shinjiro Sueda, Doug L. James, and Dinesh K. Pai. 2008. Staggered Projections for Frictional Contact in Multibody Systems. *ACM Trans. Graph.* 27, 5, Article 164 (dec 2008), 11 pages. <https://doi.org/10.1145/1409060.1409117>
- Kurt Leimer and Przemyslaw Musalski. 2020. Reduced-Order Simulation of Flexible Meta-Materials. *Proceedings - SCF 2020: ACM Symposium on Computational Fabrication*. <https://doi.org/10.1145/3424630.3425411>
- Samuel Lensgraf, Karim Itani, Yinan Zhang, Zezhou Sun, Yijia Wu, Alberto Quattrini Li, Bo Zhu, Emily Whiting, Weifu Wang, and Devin J. Balkcom. 2020. PuzzleFlex: kinematic motion of chains with loose joints. In *2020 IEEE International Conference on Robotics and Automation, ICRA 2020, Paris, France, May 31 - August 31, 2020*. IEEE, 6730–6737. <https://doi.org/10.1109/ICRA40945.2020.9196854>
- Minchen Li, Zachary Ferguson, Teseo Schneider, Timothy Langlois, Denis Zorin, Daniele Panozzo, Chenfanfu Jiang, and Danny M. Kaufman. 2020. Incremental potential contact: intersection-and inversion-free, large-deformation dynamics. *ACM Trans. Graph.* 39, 4, Article 49 (Aug. 2020), 20 pages. <https://doi.org/10.1145/3386569.3392425>
- Minchen Li, Zachary Ferguson, Teseo Schneider, Timothy Langlois, Denis Zorin, Daniele Panozzo, Chenfanfu Jiang, and Danny M. Kaufman. 2023b. Convergent Incremental Potential Contact. *arXiv preprint arXiv:2307.15908* (2023).
- Yue Li, Stelian Coros, and Bernhard Thomaszewski. 2023a. Neural Metamaterial Networks for Nonlinear Material Design. *ACM Trans. Graph.* 42, 6, Article 186 (Dec. 2023), 13 pages. <https://doi.org/10.1145/3618325>
- Yifei Li, Tao Du, Kui Wu, Jie Xu, and Wojciech Matusik. 2022. DiffCloth: Differentiable Cloth Simulation with Dry Frictional Contact. *ACM Trans. Graph.* 42, 1, Article 2 (oct 2022), 20 pages. <https://doi.org/10.1145/3527660>
- Lin Lu, Andrei Sharf, Haisen Zhao, Yuan Wei, Qingnan Fan, Xuelin Chen, Yann Savoye, Changhe Tu, Daniel Cohen-Or, and Baqao Chen. 2014. Build-to-Last: Strength to Weight 3D Printed Objects. *ACM Trans. Graph.* 33, 4, Article 97 (jul 2014), 10 pages. <https://doi.org/10.1145/2601097.2601168>
- Jonás Martínez, Jérémie Dumas, and Sylvain Lefebvre. 2016. Procedural voronoi foams for additive manufacturing. *ACM Trans. Graph.* 35, 4, Article 44 (July 2016), 12 pages. <https://doi.org/10.1145/2897824.2925922>
- Jonás Martínez, Méline Skouras, Christian Schumacher, Samuel Hornus, Sylvain Lefebvre, and Bernhard Thomaszewski. 2019. Star-shaped metrics for mechanical metamaterial design. *ACM Trans. Graph.* 38, 4, Article 82 (July 2019), 13 pages. <https://doi.org/10.1145/3306346.3322989>
- Jonás Martínez, Haichuan Song, Jérémie Dumas, and Sylvain Lefebvre. 2017. Orthotropic k-nearest foams for additive manufacturing. *ACM Trans. Graph.* 36, 4, Article 121 (July 2017), 12 pages. <https://doi.org/10.1145/3072959.3073638>
- Juan Sebastian Montes Maestre, Yinwei Du, Ronan Hinche, Stelian Coros, and Bernhard Thomaszewski. 2024. FlexScale: Modeling and Characterization of Flexible Scaled Sheets. *ACM Trans. Graph.* 43, 4, Article 86 (July 2024), 14 pages. <https://doi.org/10.1145/3658175>
- Julian Panetta, Abtin Rahimian, and Denis Zorin. 2017. Worst-case stress relief for microstructures. *ACM Trans. Graph.* 36, 4, Article 122 (July 2017), 16 pages. <https://doi.org/10.1145/3072959.3073649>

- Julian Panetta, Qingnan Zhou, Luigi Malomo, Nico Pietroni, Paolo Cignoni, and Denis Zorin. 2015. Elastic textures for additive fabrication. *ACM Trans. Graph.* 34, 4, Article 135 (July 2015), 12 pages. <https://doi.org/10.1145/2766937>
- Albert Peiret, Sheldon Andrews, József Kövecses, Paul G. Kry, and Marek Teichmann. 2019. Schur Complement-Based Substructuring of Stiff Multibody Systems with Contact. *ACM Trans. Graph.* 38, 5, Article 150 (oct 2019), 17 pages. <https://doi.org/10.1145/3355621>
- Ante Qu and Doug L. James. 2021. Fast Linking Numbers for Topology Verification of Loopy Structures. *ACM Trans. Graph.* 40, 4, Article 106 (jul 2021), 19 pages. <https://doi.org/10.1145/3450626.3459778>
- Mark Ransley, Peter Smitham, and Mark Miodownik. 2017. Active chainmail fabrics for soft robotic applications. *Smart Materials and Structures* 26, 8 (jul 2017), 08LT02. <https://doi.org/10.1088/1361-665X/aa7221>
- Yingying Ren, Julian Panetta, Seiichi Suzuki, Uday Kusupati, Florin Isvoranu, and Mark Pauly. 2024. Computational Homogenization for Inverse Design of Surface-based Inflatables. *ACM Trans. Graph.* 43, 4, Article 87 (July 2024), 18 pages. <https://doi.org/10.1145/3658125>
- Emmanuel Rodriguez, Georges-Pierre Bonneau, Stefanie Hahmann, and Mélina Skouras. 2022. Computational Design of Laser-Cut Bending-Active Structures. *Computer-Aided Design* 151 (2022), 103335. <https://doi.org/10.1016/j.cad.2022.103335>
- Christian Schumacher, Bernd Bickel, Jan Rys, Steve Marschner, Chiara Daraio, and Markus Gross. 2015. Microstructures to control elasticity in 3D printing. *ACM Trans. Graph.* 34, 4, Article 136 (July 2015), 13 pages. <https://doi.org/10.1145/2766926>
- Christian Schumacher, Steve Marschner, Markus Gross, and Bernhard Thomaszewski. 2018. Mechanical characterization of structured sheet materials. *ACM Trans. Graph.* 37, 4, Article 148 (July 2018), 15 pages. <https://doi.org/10.1145/3197517.3201278>
- Mélina Skouras, Stelian Coros, Eitan Grinspun, and Bernhard Thomaszewski. 2015. Interactive Surface Design with Interlocking Elements. *ACM Trans. Graph.* 34, 6, Article 224 (nov 2015), 7 pages. <https://doi.org/10.1145/2816795.2818128>
- Mélina Skouras, Bernhard Thomaszewski, Stelian Coros, Bernd Bickel, and Markus Gross. 2013. Computational design of actuated deformable characters. *ACM Trans. Graph.* 32, 4, Article 82 (July 2013), 10 pages. <https://doi.org/10.1145/2461912.2461979>
- Peng Song, Chi-Wing Fu, and Daniel Cohen-Or. 2012. Recursive Interlocking Puzzles. *ACM Trans. Graph.* 31, 6, Article 128 (nov 2012), 10 pages. <https://doi.org/10.1145/2366145.2366147>
- Peng Song, Chi-Wing Fu, Yueming Jin, Hongfei Xu, Ligang Liu, Pheng-Ann Heng, and Daniel Cohen-Or. 2017. Reconfigurable Interlocking Furniture. *ACM Trans. Graph.* 36, 6, Article 174 (nov 2017), 14 pages. <https://doi.org/10.1145/3130800.3130803>
- Ondrej Stava, Juraj Vanek, Bedrich Benes, Nathan Carr, and Radomír Měch. 2012. Stress relief: improving structural strength of 3D printable objects. *ACM Trans. Graph.* 31, 4, Article 48 (July 2012), 11 pages. <https://doi.org/10.1145/2185520.2185544>
- Timothy Sun and Changxi Zheng. 2015. Computational design of twisty joints and puzzles. *ACM Trans. Graph.* 34, 4, Article 101 (July 2015), 11 pages. <https://doi.org/10.1145/2766961>
- Zezhou Sun, Devin Balkcom, and Emily Whiting. 2024. StructCurves: Interlocking Block-Based Line Structures. In *Proceedings of the 37th Annual ACM Symposium on User Interface Software and Technology* (Pittsburgh, PA, USA) (*UIST ’24*). Association for Computing Machinery, New York, NY, USA, Article 39, 11 pages. <https://doi.org/10.1145/3654777.3676354>
- Pengbin Tang, Stelian Coros, and Bernhard Thomaszewski. 2023. Beyond Chainmail: Computational Modeling of Discrete Interlocking Materials. *ACM Trans. Graph.* 42, 4, Article 84 (July 2023), 12 pages. <https://doi.org/10.1145/3592112>
- Bernhard Thomaszewski, Stelian Coros, Damien Gauge, Vittorio Megaro, Eitan Grinspun, and Markus Gross. 2014. Computational Design of Linkage-Based Characters. *ACM Trans. Graph.* 33, 4, Article 64 (jul 2014), 9 pages. <https://doi.org/10.1145/2601097.2601143>
- Yuanyuan Tian, Kaijuan Chen, Han Zheng, Devesh R. Kripalani, Zhuohong Zeng, Asker Jarlöv, Jiayao Chen, Lichun Bai, Adrian Ong, Hejun Du, Guozheng Kang, Qihong Fang, Lihua Zhao, H. Jerry Qi, Yifan Wang, and Kun Zhou. 2023. Additively Manufactured Dual-Faced Structured Fabric for Shape-Adaptive Protection. *Advanced Science* 10, 21 (2023), 2301567. <https://doi.org/10.1002/advs.202301567> arXiv:<https://advanced.onlinelibrary.wiley.com/doi/pdf/10.1002/advs.202301567>
- Davi Colli Tozoni, Jérémie Dumas, Zhongshi Jiang, Julian Panetta, Daniela Panozzo, and Denis Zorin. 2020. A low-parametric rhombic microstructure family for irregular lattices. *ACM Trans. Graph.* 39, 4, Article 101 (Aug. 2020), 20 pages. <https://doi.org/10.1145/3386569.3392451>
- Guohui Wang, Haili Wang, Weinan Gao, Xudong Yang, and Yifan Wang. 2023. Jamming Enabled Variable Stiffness Wrist Exoskeleton for Tremor Suppression. *IEEE Robotics and Automation Letters* 8, 6 (2023), 3693–3700. <https://doi.org/10.1109/LRA.2023.3270747>
- Yifan Wang, Liuchi Li, Douglas Hofmann, José E Andrade, and Chiara Daraio. 2021. Structured fabrics with tunable mechanical properties. *Nature* 596, 7871 (2021), 238–243.
- Ziqi Wang, Peng Song, Florin Isvoranu, and Mark Pauly. 2019. Design and Structural Optimization of Topological Interlocking Assemblies. *ACM Trans. Graph.* 38, 6, Article 193 (nov 2019), 13 pages. <https://doi.org/10.1145/3355089.3356489>
- Ziqi Wang, Peng Song, and Mark Pauly. 2018. DESIA: A General Framework for Designing Interlocking Assemblies. *ACM Trans. Graph.* 37, 6, Article 191 (dec 2018), 14 pages. <https://doi.org/10.1145/3272127.3275034>
- Shiqing Xin, Chi-Fu Lai, Chi-Wing Fu, Tien-Tsin Wong, Ying He, and Daniel Cohen-Or. 2011. Making Burr Puzzles from 3D Models. *ACM Trans. Graph.* 30, 4, Article 97 (jul 2011), 8 pages. <https://doi.org/10.1145/2010324.1964992>
- Jiaxian Yao, Danny M. Kaufman, Yotam Gingold, and Maneesh Agrawala. 2017. Interactive Design and Stability Analysis of Decorative Joinery for Furniture. *ACM Trans. Graph.* 36, 2, Article 20 (mar 2017), 16 pages. <https://doi.org/10.1145/3054740>
- Qingnan Zhou, Julian Panetta, and Denis Zorin. 2013. Worst-case structural analysis. *ACM Trans. Graph.* 32, 4, Article 137 (July 2013), 12 pages. <https://doi.org/10.1145/2461912.2461967>
- Wenjie Zhou, Sujeeka Nadarajah, Liuchi Li, Anna Guell Izard, Hujie Yan, Aashutosh K Prachet, Payal Patel, Xiaoxing Xia, and Chiara Daraio. 2025. 3D polycatenated architected materials. *Science* 387, 6731 (2025), 269–277.
- Bo Zhu, Mélina Skouras, Desai Chen, and Wojciech Matusik. 2017. Two-Scale Topology Optimization with Microstructures. *ACM Trans. Graph.* 36, 4, Article 120b (jul 2017), 16 pages. <https://doi.org/10.1145/3072959.3095815>
- Lifeng Zhu, Weiwei Xu, John Snyder, Yang Liu, Guoping Wang, and Baining Guo. 2012. Motion-guided mechanical toy modeling. *ACM Trans. Graph.* 31, 6, Article 127 (Nov. 2012), 10 pages. <https://doi.org/10.1145/2366145.2366146>